Title

The frequency gradient of human resting-state brain oscillations follows cortical hierarchies.

Author names and affiliations

Keyvan Mahjoory[1]*, Jan-Mathijs Schoffelen[2], Anne Keitel[3], Joachim Gross[1,4,5]*

Correspondence:

kmahjoory@gmail.com (K.M.); joachim.gross@uni-muenster.de (J.G.)

[1]Institute for Biomagnetism and Biosignalanalysis (IBB), University of Muenster, 48149, Muenster, Germany.

[2]Radboud University Nijmegen, Donders Institute for Brain, Cognition and Behaviour, Nijmegen, The Netherlands.

[3]Psychology, University of Dundee, Scrymgeour Building, Dundee DD1 4HN, UK

[4]Centre for Cognitive Neuroimaging (CCNi), University of Glasgow, Glasgow, UK

[5]Otto-Creutzfeldt-Center for Cognitive and Behavioral Neuroscience, University of Muenster, 48149 Muenster, Germany.

Abstract

The human cortex is characterized by local morphological features such as cortical thickness, myelin content and gene expression that change along the posterior-anterior axis. We investigated if these structural gradients are associated with a similar gradient in a prominent feature of brain activity - namely the frequency of brain oscillations. In resting-state MEG recordings from healthy participants (N=187), we found that the strongest peak frequency in a brain area decreases significantly, gradually and robustly along the posterior-anterior axis following the global hierarchy from early sensory to higher-order areas. This spatial gradient of peak frequency was significantly anticorrelated with the cortical thickness of corresponding areas representing a proxy of the cortical hierarchical level. This result indicates that the intrinsic 'resonance' frequency decreases systematically from early sensory to higher-order areas and establishes a new structure-function relationship pertaining to brain oscillations as a core organizational principle that may underlie hierarchical specialization in the brain.

Introduction

It is well established that the brain's cortical areas differ in their cyto- and myeloarchitectonic structure, local and long range anatomical connectivity, activity and, by consequence, their function (Glasser et al., 2016; Huntenburg et al., 2017). Interestingly, many structural features that distinguish individual brain areas change gradually in an orderly manner across the cortex, leading to spatial gradients of features. The most prominent and best established gradients are evident along the posterior-anterior axis (Eickhoff et al., 2018; Felleman and Van Essen, 1991; Huntenburg et al., 2018). For instance, neuron density decreases and neuronal connectivity increases from posterior to anterior brain areas. These differences have been attributed to differences in neurogenesis for posterior compared to anterior brain areas (Hill et al., 2010;

Huntenburg et al., 2018). A similar posterior-anterior gradient has been observed for myelin content, cortical thickness, and gene expression (Burt et al., 2018). Next to the posterior-anterior gradient, other global spatial organization principles have been proposed to explain the variation of microstructural features across the cortex. For instance, Huntenburg et al. suggest a sensorimotor to transmodal gradient as an important intrinsic organizing dimension of human cortex (Huntenburg et al., 2018) reflecting gradual changes in structural features from functionally unimodal (dedicated sensory or motor) areas to higher order, transmodal areas.

In addition to structural gradients as an organizing principle reflecting global cortical organization, it is well acknowledged that cortical areas are structurally connected into larger networks, which often display a hierarchical organization. Cortical hierarchies are typically established based on the degree of microstructural differentiation of the connected areas, and on the classification of the anatomical connections as feedforward or feedback using histological tract-tracing. Early sensory areas with predominantly feedforward outgoing connections are placed at the bottom of the hierarchy and higher order association areas with mostly feedback outgoing connections are placed at the top of the hierarchy (Felleman and Van Essen, 1991; Markov et al., 2014). A noninvasive, but indirect index of these hierarchies is cortical thickness, a macroscopic feature of the cortex, which can be estimated from MRI scans. It has been shown that cortical thickness mirrors global hierarchical organization of the cortex as well as local hierarchies in visual, auditory and somatosensory areas (Jasmin et al., 2019; Wagstyl et al., 2015), and, therefore, could be used as a basis for understanding hierarchy-gradient relationships in the cortex.

The presence of these anatomical gradients raises the question to what extent they are reflected in features of brain activity and brain function. Indeed, it has been shown that cortical areas follow a hierarchical ordering in their timescales of intrinsic fluctuations as for example measured in the autocorrelation of spiking activity (Murray et al., 2014).

Sensory areas show faster fluctuations while frontal areas show slower fluctuations. Shorter timescales in sensory areas enables them to reflect dynamic changes in the environment, whereas the longer timescales in prefrontal areas allows for integration of information. Particularly, this gradient of 'temporal receptive windows' has been demonstrated in visual (Himberger et al., 2018) and auditory processing (Jasmin et al., 2019) and could be related to the frequency of spontaneous brain oscillations. Oscillations are a prominent feature of brain activity, and have been suggested to play a central role in coordinating neuronal activity (Fries, 2005; Wang, 2010). Similar to many anatomical features described above, the spectral activity patterns seem to be characteristic for each brain area (Keitel and Gross, 2016). This is consistent with the view that the individual anatomical structure of a brain area shapes its rhythmic neuronal activity, which led us to hypothesize the existence of a posterior-anterior gradient in the frequency of spontaneous brain rhythms.

Spontaneous rhythms have been studied in the past but typically by focusing on the power in specific frequency bands (Hillebrand et al., 2016; Keitel and Gross, 2016; Mellem et al., 2017). Overall, these MEG studies revealed strongest cortical generators for the dominant alpha rhythm (7-13 Hz) in occipito-parietal brain areas. The beta band (15-30 Hz) shows strongest activity in sensorimotor areas while delta (1-3 Hz) and theta (3-7 Hz) bands are associated with activity in wide-spread areas including frontal cortex. Here, we adopt a different approach that is based on sophisticated identification of spectral peaks in the power spectra of source-localized resting-state MEG data and included modelling of the 1/f spectral background (Haller et al., 2018). This approach offers two distinct advantages. First, focusing on spectral peaks ensures that results are indeed based on brain oscillations. This is not necessarily the case when using the power in a pre-defined frequency band or using band-pass filtered data. Second, by explicitly modelling the 1/f spectral background across the entire cortex we can dissociate

contributions due to aperiodic neuronal background activity from those originating from oscillatory activity.

We used this approach to specifically test the hypothesis of a posterior-anterior gradient in the frequency of spontaneous brain rhythms. We identified the frequencies of the dominant brain rhythm across the cortex in source-localized resting-state MEG data of 187 individuals.

As we describe below, we found a spatial gradient of peak frequency across the cortex following the cortical hierarchy.

Results

Spatial Gradients of the Dominant Peak Frequency of Oscillations

We analyzed publicly available resting-state MEG data from 187 participants (J.-M. Schoffelen et al., 2019; J. M. Schoffelen et al., 2019), reconstructing cortical activity time courses for 384 regions-of-interest (ROIs) on the cortical surface. This cortical parcellation (introduced in (Schoffelen et al., 2017)) was constructed from the Conte69 atlas (Van Essen et al., 2012) which divides the cortical surface according to the division introduced by Brodmann (Brodmann, 1909). From the estimated activity time courses, we obtained the power spectrum for each ROI and individual, and identified spectral peaks after fitting and subtracting the arrhythmic 1/f component (see Figure 1A and method section). Subsequently, we identified for each participant and ROI the spectral peak with strongest amplitude in the original power spectrum (peak frequency (PF)). We used PF to test our hypothesis of a posterior-anterior frequency gradient. Figure 1B, top panel, shows the distribution of PF as a function of the ROI's location along the y-axis of the coordinate system (posterior to anterior). Each point represents the trimmed mean across participants of the PF for one ROI. A clear gradual decrease of PF from posterior to anterior is evident and supported by a significant robust correlation (Robust Correlation Toolbox) (Pernet et al., 2012) between the PF and the ROI's y-coordinate ($r = -0.84$, p

<< 0.001). This frequency gradient is also evident in the cortical maps that show the trimmed mean of the PF across participants for the 384 ROIs (Figure 1B, bottom panel). Next, we used linear mixed effect modelling (LMEM) for statistics, in order to model the spatial gradients of PF, while accounting for interindividual variability. We used PF as the response variable, and the coordinates of the ROI centroids (X: left to right, Y: posterior to anterior, and Z: inferior to superior) plus their two-way interactions set as fixed effects. We modelled the individual slope and offset as random effects to account for variability between participants. The fixed effect parameters capture mean-variation in the PF that is shared by all individuals (see Methods section), while the participant-unique variance of the PF is addressed by random effects. Thus, our model provides a robust and comprehensive characterization of spatial changes of PF across the cortex. Figure 1C displays a table of T-values for fixed-effect parameters of LMEM and the modelled PF on the cortex. LMEM yielded highly significant scores for Y ($t = -15.6$, $p << 0.001$), Z ($t = -10.4$, $p << 0.001$), and Y:Z ($t = -32$, $p << 0.001$) directions. Together, these results support the conclusion that the peak frequency of brain oscillations decreases systematically in posterior-anterior direction.

On the basis of the observed frequency gradient, the question may arise, whether the spatial pattern of frequency across the cortex is the result of spatial leakage originating from an occipital alpha and frontal theta source. If this is the case, we would not expect to see significant frequency change in areas close to primary visual area (V1). To address this question, we computed the geodesic distance between V1 and all areas located 0.5–1.5cm away from V1, and applied linear mixed effect modelling of PF as a function of the distance values. We found a significant negative correlation between PF and distance ($t = -18.45$, $p << 0.001$). This demonstrates a significant frequency gradient already in occipital brain areas where the spatial leakage effect of a potential frontal theta source is negligible. Overall, this control analysis supports the existence of a genuine gradual change of PF across the cortex.

148

149 ======== Figure 1 about here ========

150

151 **Spatial Gradients of Spectral Properties of the 1/f Signal**

152 Neurophysiological signals typically consist of oscillatory signal components with distinct
153 spectral peaks, embedded in an arrhythmic 1/f signal component. Variation in the
154 properties of this 1/f component may give rise to shifts of spectral peak estimates, and
155 lead to misidentification of peak frequencies (Haller et al., 2018). To investigate this
156 issue, we examined the spatial distribution across the cortex of the estimated slope and
157 offset parameters of the arrhythmic component (see method section), using LME
158 modelling. As illustrated in figures 2A and 2B, we found significant scores for Y (slope: t
159 = -4.3 , $p << 0.001$; offset: $t = 2.8$, $p < 0.01$) , Y:Z (slope: $t = 6.9$, $p << 0.001$; offset: $t =$
160 13.2, $p << 0.001$), and X:Y (slope: $t = -6.8$, $p << 0.001$; offset: $t = -5.8$, $p << 0.001$)
161 directions. These results indicate a significant decrease of the 1/f slope, and an increase
162 of its offset along the posterior-to-anterior direction. The observed similarity between
163 spatial patterns of 1/f parameters and PF, brings up the question to what extent these
164 parameters could contribute to the observed PF gradient. To assess this, we tested to
165 what extent the spatial change of PF is independent of spatial changes of 1/f slope and
166 offset. We thus used LMEM and regressed out the linear contribution of 1/f slope and
167 offset to PF. After doing this we again used LMEM to model the residual PF values as a
168 function of spatial coordinates. The results confirmed a significant posterior-anterior
169 gradient of residual PF values (t-values: Y = -8.3, Z = -4.3, Y:Z = -16; all $p << 0.001$,
170 Figures 2C and 2D). We therefore conclude that the posterior-anterior PF gradient is
171 largely independent of the observed gradients of slope and offset of the 1/f component.

172

173 ======== Figure 2 about here ========

174

Frequency Gradients and Cortical Hierarchies

The visual system's cortical hierarchy largely progresses along the posterior-anterior direction, and starts in early visual areas in occipital cortex and progresses along the dorsal and ventral streams to anterior areas. Since this progression of cortical hierarchical level coincides with the observed gradient in PF, we tested the hypothesis that the PF gradient is more closely related to cortical hierarchical level than to spatial location. We used cortical thickness (CT) as a proxy for the quantification of the hierarchical level of brain areas (Wagstyl et al., 2015).

We used Freesurfer to estimate CT as the shortest distance between corresponding vertices on the white matter surface and the pial surface. To obtain a thickness value for each cortical region, the individual thickness scores were averaged across vertices of that region. Robust correlation demonstrated a significant change of mean CT along the posterior-anterior axis ($r = 0.36$, $p<<0.001$, Figure 3A top panel). Figure 3A, the bottom panel depicts CT values averaged across participants and mapped on the cortex. LMEM of CT as a function of ROI coordinates showed a significant and progressive increase of CT from posterior to anterior regions (t-values: Y = 49.73, Z = -29.26, Y:Z = 16.23; all $p << 0.001$). Having established the significant posterior-anterior increase of CT, we then tested for a significant relationship between CT and PF. Robust correlation ($r = -0.14$, $p < 0.001$, Figure 3B) and LMEM ($t = -13.8$, $p << 0.001$) showed a significant negative relationship between PF and CT. Next, we asked the question if this relationship is still significant after removing from both, PF and CT, the effect of ROI coordinates (x,y,z). This was done by modeling the dependencies of PF and CT respectively on ROI coordinates and computing the residuals PFres and CTres. These residuals describe individual spatial variations of PF and CT that cannot be explained by a linear model of their spatial location. PFres and CTres are still significantly related (LMEM: $t = -6.9$, $p << 0.001$, Figure 3C) indicating that they are more directly related to each other than can be

explained by their individual dependency on location (x,y,z). This result suggests that peak frequency is related to structural features that likely represent cortical hierarchies.

======== Figure 3 about here ========

We further tested the relationship between PF gradients and cortical hierarchies along the anatomically defined and well-established visual hierarchy. Following an approach by Michalareas et al. (Michalareas et al., 2016), we selected seven cortical regions showing strong homology to macaques visual areas (V1, V2, V4, MT, DP, TEO, 7A) using the cortical parcellation of Glasser et al. (Glasser et al., 2016). We modelled spatial changes of PF along the visual hierarchy, using LMEM (see method section for details), and found a significant decrease of PF ($t = -10.1$, $p << 0.001$) and a significant increase of CT ($t = 54.9$, $p << 0.001$, Figure 4A).

Previous studies have shown that cortical regions can be contextualized in terms of eight canonical resting-state networks (RSNs) comprising three sensory ('VIS': visual, 'SOM': somatosensory, and 'AUD': auditory) and five higher-order association networks ('FPN': frontoparietal, 'CON': cingulo-opercular, 'DMN': default mode, 'DAN': dorsal attention, and 'VAN': ventral attention; Figure 4B)(Ito et al., 2017). Markers of hierarchical microcircuit specialization such as the ratio of T1-weighted to T2-weighted MRI maps (T1w/T2w) are significantly different between sensory and association areas (Burt et al., 2018; Demirtaş et al., 2019). Here, we extended this approach to our measures to test for differences in PF/CT between sensory and association networks. Following Ito et al. (Ito et al., 2017) we assigned all areas to eight networks. We then averaged PF and CT scores within ROIs of each network, and applied LMEM to test the effect of the network on PF and CT organization. For LMEM we defined the fixed effect as a categorical variable comprising eight labels corresponding to RSNs. Next, we applied ANOVA on LMEM fit and found a significant effect of RSNs for CT and PF (PF: F-stats = 264, $p <<$

0.001; CT: F-stats = 746, p << 0.001). To test whether PF and CT variation follows the sensory-association axis, we used LMEM, with networks designated to 'sensory' and 'association' categories (PF: t = -11.1, p << 0.001; CT: t = 14.7, p << 0.001, Figure 4C). Similar to the significant difference of T1w/T2w between sensory and association networks we also see significant differences in PF and CT. As expected PF is higher in sensory areas compared to association areas while an opposite effect is observed for CT.

======== Figure 4 about here ========

Characterizing Band-specific PF and Spatial Gradients

In the results presented so far, we defined the PF per ROI, as the most prominent band-limited peak in the spectrum. Multiple ROIs, however, showed more than a single spectral peak. Figure 5 shows a histogram (across ROIs and participants) of all detected spectral peaks. This histogram of peak frequencies clearly delineates the classical frequency bands that are used in the EEG and MEG literature (4–7.5 (theta), 8.5–13 (alpha), 15–25 (low beta) 27.5–34 (high beta)). Defining the theta, alpha and beta frequency bands based on the histogram, we determined for each ROI and participant the band-specific PF (BS-PF). Next, we modelled the spatial distribution of BS-PFs across the cortex, similar to the analysis shown above. Analogous to the PF analysis, we used LMEM to model BS-PF as a function of the ROIs' coordinates. We found a significant decrease of alpha peak frequency (Y, t = -10, p << .0.001; = Y:Z, t = 3.2, p = 0.001, supplementary figures S1A and S1B) along the posterior-to-anterior direction, whereas theta (Y, t = 7.4, p << .0.001; Z, t = -7, p << 0.001; Y:Z, t = -8, p << 0.001, supplementary figures S2A and S3B) and beta (Y, t = 11.5, p << 0.001; Z, t = 5.6, p << 0.001; Y:Z, t = 20, p << 0.001, supplementary figures S3A and S3B) frequencies significantly increased along the same direction.

255

256 ======== Figure 5 about here ========

257

258 Discussion

259 This study is the first comprehensive demonstration of frequency gradients across the
260 human cortex using a large set of resting-state MEG recordings. We found that the
261 strongest peak frequency in a brain area decreases significantly, gradually and robustly
262 along the posterior-anterior axis, following the global cortical hierarchy from early sensory
263 to higher order areas. This finding establishes a frequency gradient of resting-state brain
264 rhythms that complements previous anatomical studies reporting a posterior-anterior
265 gradient in microscale and macroscale anatomical features of animal and human cortex
266 (Huntenburg et al., 2018). This gradient is consistent with a recent invasive study
267 showing a systematic decrease of peak frequency from posterior to anterior brain areas
268 in ECoG recordings of epilepsy patients (Zhang et al., 2018). Chiang et al. suggested a
269 similar frequency decrease albeit only based on 19-electrode EEG (Chiang et al., 2011).
270 A differentiating feature of our approach was that we used a large number of healthy
271 participants (N = 187), reconstructed cortical activity from noninvasive MEG recordings,
272 and considered further anatomical features (i.e. cortical thickness). Notably, estimating
273 the power spectrum in finely parcellated ROIs allowed us an accurate and robust
274 identification of peak frequencies and characterization of their spatial gradients across
275 the entire cortical surface. Importantly, we focus on peaks in the power spectrum that
276 indicate the presence of rhythmicity in the neuronal activity, instead of focusing on
277 predefined frequency bands where these rhythms might be absent. As slope and offset
278 of frequency gradient could dramatically vary across participants, averaging across
279 participants may not yield a reliable representation of PF gradient. Instead, we used
280 mixed effect modelling of PF along the cortical hierarchies, where the between-
281 participant variability was taken into account as a random effect. Our approach

additionally revealed that cortical peak frequencies decrease systematically along the inferior-superior axis. As seen in Figure 1 this seems to result from the fact that higher-order frontal areas with lower PF have higher z-coordinates compared to the early sensory areas with higher PF.

Results of our analyses showed that, just as peak frequency significantly decreased along the posterior-anterior axis, CT significantly increased in the same direction, which resulted in a significant anticorrelation between PF and CT. The observed correlation holds after removing the effect of spatial location (x,y,z). This seems to indicate that PF and CT are more closely related to each other than can be explained by spatial location alone. Since cortical hierarchies do not strictly follow a single linear trajectory in space (e.g. posterior-anterior) our results are consistent with the idea that both PF and CT, follow cortical hierarchies. Indeed, such local spatial gradients have been reported in multiple features of cortex during auditory perception (Jasmin et al., 2019) and visual processing streams (Himberger et al., 2018). From a broader view, local gradients could mirror complex organization of gradients in human cortex and support the approach of global gradient along the sensory to transmodal areas (Huntenburg et al., 2018). On the other hand, posterior-anterior gradient of PF was significant after subtracting CT scores from PF values. This suggests a partial independence of both measures. Since PF is a measure derived from brain activity the reported gradient could be modulated dynamically depending on cognitive state or task demands. Further studies are needed to investigate this in more detail.

We further addressed the question if our results can be explained by the linear superposition of activity from an occipital alpha source and a frontal theta source. Along the posterior-anterior axis differential superposition of both sources could lead to a frequency gradient, due to imperfect unmixing of the signals. However, our analysis revealed that a significant frequency gradient is already evident within 1.5cm of V1 where the effect of a frontal theta source (which has on average a lower power compared to

occipital alpha) is negligible. Additional supporting evidence can be drawn from intracranial studies, where the data is directly recorded from cortex. Zhang et al. (Zhang et al., 2018) have shown that oscillations generally propagate in a posterior-to-anterior direction because they are coordinated by an overall decrease in intrinsic oscillation frequency from posterior to anterior regions (see figures S6 and 7 of (Zhang et al., 2018)). Overall, this indicates the existence of a gradual decrease of PF along the posterior-anterior axis.

What is the potential functional role of this frequency gradient? Zhang et al. demonstrated the existence of travelling waves along the frequency gradient (Zhang et al., 2018). Interestingly, they found that local frequencies along the posterior-anterior direction are positively correlated with waves' propagation speed and direction consistent with a proposed model of travelling waves based on weakly coupled oscillators (WCO) (Ermentrout and Kleinfeld, 2001). These travelling waves might serve to drive neural communication along the cortical hierarchy possibly through nested gamma oscillations (Bahramisharif et al., 2013). In addition, travelling waves have been associated with memory consolidation and learning (Muller et al., 2018). It is of interest to note that frequency gradients have been reported previously in the entorhinal cortex (Giocomo et al., 2011; Giocomo and Hasselmo, 2009). Here, a frequency decrease and corresponding travelling waves have been observed in the dorsal-ventral direction and have been related to a representational gradient of spatial scales from coarse to fine (Muller et al., 2018). Indeed, converging evidence across recording methods, species and cortical domains suggests that representations become more 'integrated' with decreasing 'resonance' frequency of the underlying neuronal population. A prime example is the auditory cortex where response latencies and complexity of processing increase along the posterior-anterior axis (Jasmin et al., 2019). This is also mirrored by an increase in cortical thickness and increased ratio of feedback to feedforward connections along this axis. Similar observations have been made across more widely

distributed cortical areas where timescales of intrinsic fluctuations in spiking activity increase from posterior to anterior brain areas (Murray et al., 2014). Not surprisingly, these time scales are largely determined by the time constants of synaptic transmission (Duarte et al., 2017). But interestingly, in a computational model of activity in macaque cortex using anatomical connectivity a gradient of time scales also emerges with short, transient responses to input in sensory areas and slower, sustained responses in higher-order areas (Chaudhuri et al., 2015) (see also (Kiebel et al., 2008)).

Our detailed analysis was based on the cortical ROIs' spectral peak with strongest power (PF). However, we identified all peaks in the power spectrum of each ROI. Since spectral peaks indicate the presence of brain rhythms, this data represents a comprehensive overview of these rhythms across the cortex. The histogram of spectral peaks across ROIs and participants provided a data-driven definition of frequency bands. Interestingly, the histogram delineates the classical frequency bands with histogram peaks centering at 4–7.5 (theta), 8.5–13 (alpha), 15–25 (low-beta) 27.5–34 (high-beta) (see figure 5). This is the first MEG study to our knowledge to identify frequency bands from peak frequencies in a large data set (see (Groppe et al., 2013) for a similar approach in a smaller sample of ECoG data).

We further analyzed these specific frequency bands for gradients and found significant posterior-anterior frequency changes in the theta, alpha and beta frequency band. Results in the alpha band mirrored the previous results based on the overall strongest peak frequency. Interestingly, and in contrast to the alpha band, peak frequencies increased along the posterior-anterior direction in the theta and beta frequency band. In the model used by Zhang et al. this would correspond to travelling waves from anterior to posterior brain areas (Zhang et al., 2018) that might represent frequency channels for top-down effects (Michalareas et al., 2016; Wang, 2010).

In summary, our findings show that peak frequencies of cortical areas form a spatial gradient, which follows the global posterior-anterior hierarchy as well as local anatomical

hierarchies. Previous research also points to spatial gradients in multiple features of the human and animal cortex. Further research might explore implications of frequency gradients in different cognitive states, disease, and aging.

Materials and Methods

Experimental Design

In this study we used the MOUS dataset (J.-M. Schoffelen et al., 2019; J. M. Schoffelen et al., 2019) which, among others, contains five minutes of resting state MEG recordings collected from 197 healthy participants (age: mean = 22, range = 18–32, gender: 94 females). The participants were instructed to think of nothing specific while focusing on the fixation cross at the center of the screen. Data was collected using a CTF 275-channel radial gradiometer system, and sampled at 1200 Hz (0-300 Hz bandpass), and additional 29 reference channels for noise cancellation purposes.

The anatomical images of the head were obtained with a SIEMENS Trio 3T scanner using a T1-weighted magnetization-prepared rapid gradient-echo (MP-RAGE) pulse sequence, with the following parameters: volume TR = 2300 ms, TE = 3.03 ms, 8 degree flip-angle, 1 slab, slice-matrix size = 256 × 256, slice thickness = 1 mm, field of view = 256 mm, isotropic voxel-size = 1.0 × 1.0 × 1.0 mm.

After removing 10 participants lacking sufficient data quality, we used 187 participants for our analyses.

MEG Preprocessing

All analyses were performed using custom-written Matlab (MathWorks, Inc, Natick, Massachusetts, USA) scripts and the Fieldtrip package (Oostenveld et al., 2011). Gradiometer signals were converted to synthetic third-order gradients, high-pass filtered at 0.5 Hz, and low-pass filtered at 140 Hz (Butterworth, 4th order). Line noise was rejected using a DFT filter at 50 and 100 Hz. After downsampling the data to 300 Hz, outlier channels/time segments were rejected using visual inspection of their time course,

spectrum and topography. Next, we used independent component analysis (ICA) to identify and remove signal components related to eye blinks/movements and cardiac activity. To this end, we performed ICA, using the infomax algorithm (Bell and Sejnowski, 1995), on a 30-dimensional signal subspace, for computational efficiency. ICs related to artifacts were identified based on their spatial topography and signal time course, and the identified spatial topographies were projected out of the sensor data. This resulted in 3.7 components on average to be rejected (range 1–6).

MRI Analysis

From T1-weighted anatomical images of participants, brain/skull boundary and cortical surfaces (white matter and pial matter) were generated using SPM (Penny et al., 2011) and Freesurfer (version 5.1)(http://surfer.nmr.mgh.harvard.edu). The cortical surface was coregistered to a template with a surface-based coregistration approach (Caret software, http://brainvis.wustl.edu/wiki/index.php/Caret:Download), and downsampled to 8,196 vertices (MNE software, martinos.org/mne/stable/index.html). Using the Caret software, the mid-thickness mesh was generated to be average of the white and pial matter surfaces. The mid-thickness surface was parceled into 384 ROIs (192 per hemisphere) according to Schoffelen et al. (Schoffelen et al., 2017).

The centroid of each parcel was specified as the vertex located at minimum geodesic distance from all other vertices of that parcel.

Source Reconstruction

Source reconstruction was performed using the linearly constrained minimum variance beamformer approach (Van Veen et al., 1997), where the lambda regularization parameter was set to 5%. This approach estimates a spatial filter for each location of a set of defined dipole locations (here: each of the 7,548 non-midline vertices of the mid-thickness cortical mesh), based on the forward model of that location and the sensor covariance matrix. The forward model was computed using the ‘singleshell’ method, with

the brain/skull boundary as volume conduction model of the head. The sensor covariance matrix was computed from two-second trials and averaged across trials.

ROI Spectrum

For each ROI, we concatenated the source time courses of the vertices belonging to that ROI, and reduced the dimensionality, using a singular value decomposition. About 15 components per ROI were retained, explaining at least 95% of the initial variance. Component time courses were segmented to two-second epochs. Power spectra were computed using a multitapered Fast Fourier transform, using discrete prolate spheroidal sequences (dpss) as windowing function, with 2 Hz spectral smoothing. To obtain a single spectrum for each ROI (ROI spectrum), we pooled spectra of epochs across components and computed the 10% trimmed mean across them. Averaging after leaving out 10% of data from left and right tails of the spectra distribution offers a more robust estimate.

Peak Frequency (PF) Detection

We estimated 1/f component of spectrum between 3 and 45 Hz using the FOOOF algorithm (Haller et al., 2018). The algorithm fits a linear approximation of 1/f in log-log spectrum and computes the corresponding slope and offset parameters. Next, we subtracted the estimated 1/f component from the spectrum to obtain a 1/f corrected spectrum per ROI. To identify spectral peaks, we used the MATLAB “findpeaks” function. We extracted all peaks but most of the analysis is based on the peak frequency with the strongest power in the original spectrum that includes the 1/f background.

Cortical Thickness (CT)

We used the Freesurfer package to obtain estimates of CT scores. The CT value of a vertex was computed as the distance between corresponding white matter and pial surface vertices. To obtain thickness values of a ROI, we averaged CT across the vertices of that ROI.

Statistical Analysis

As described above, we computed PF values for 384 ROIs (197 ROIs per hemisphere) of 187 participants. In our statistical analyses, we aimed to investigate the spatial/hierarchical organization of PF across the human cortex, but also control for the between-participant variability. To meet this purpose, we used linear mixed effect modeling (LMEM). The distinctive feature of LMEMs is that a response variable is modeled as a linear combination of 1) population characteristics that are assumed to be shared by all individuals (fixed effects), and 2) participant-specific effects, that are unique to a particular individual in the population (random effects).

To investigate the spatial organization of PFs across the cortex, we specified the PF as response variable and the coordinates of ROI centroids (X: left to right, Y: posterior to anterior, and Z: inferior to superior) plus their two-way interactions (XY, XZ, YX) as fixed effects. The inclusion of two-way interaction as predictors allows the model to adapt well to the cortex geometry. As our random structure, we nested the PFs within participants as well as within hemispheres to account for the variability between participants and hemispheres. Equation 1 shows the specified LMEM

$$PF_j = \beta_0 + S_{0j} + (\beta_1 + S_{1j})X + (\beta_2 + S_{2j})Y + (\beta_3 + S_{3j})Z + \beta_4 XY + \beta_5 XZ + \beta_6 YZ + e_j \quad (1)$$

where the response variable PF for the participant j is related to baseline level via (β_0), to ROI centroids (fixed effects) via ($\beta_i, i \in \{1,2,...,6\}$), and to error ($e_j \sim N(0,\sigma^2)$). To address the variation of predictors for participant j, we specified both random intercepts (S_{0j}) and slopes ($S_{ij}, i \in \{1,2,3\}$) for random effects. For the sake of model simplicity, no random effect was specified for two-way interactions. We estimated the fixed effect predictions for a ROI located at centroid coordinates of (x, y, z) as follows

$$PF_{xyz} = \beta_0 + \beta_1 x + \beta_2 y + \beta_3 z + \beta_4 xy + \beta_5 xz + \beta_6 yz \quad (2)$$

In our analysis we included only significant predictors for equation 2. We used an analogous approach, to test the significance of spatial changes of CT and 1/f parameters across the cortex.

To examine if the spatial distribution of PF across the cortex is independent of the spatial changes of 1/f parameters (slope and offset), we fitted a LMEM, where we set the PF as a response variable, the 1/f slope and offset scores as fixed effects, and the between-participant and hemisphere as random effects. Prior to LMEM, we standardized the PF, 1/f slope and offset scores for each participant by subtracting mean and dividing by standard deviation (z-score). Next, we estimated the coefficients for the fixed effects (1/f parameters) and regressed them out to obtain the residual PF (PFres) scores, which reflect a subspace of PF that cannot be explained by 1/f parameters. We again modeled the obtained PFres scores as a function of ROI centroids as described above (see equation 1).

To obtain the correlation between PF and CT scores, we initially computed 10% trimmed mean across participants for each ROI and performed the robust correlation (Pernet et al., 2012) between the trimmed mean values. To address the between-participant variability, we first standardized PF and CT scores (as described above), and conducted LMEM, where we specified the PF as response variable and the CT as a fixed effect predictor. The random effect was set according to equation 1. Moreover, we aimed to obtain a correlation value between PF and CT that is independent of spatial location. We first applied LMEM separately for PF and CT, modeling each as a function of ROI coordinates (see equation 1), and computed the corresponding residuals (PFres and CTres) for each ROI and participant. Subsequently, we applied LMEM between PFres and CTres values (analogous to PF and CT).

To test for the significance of PF changes along the established visual hierarchy comprising seven regions (V1, V2, V4, MT, DP, TEO, 7A), chosen according to Michalareas et al. (Michalareas et al., 2016), we used an LMEM. To impose the

hierarchical order of those seven ROIs in our LMEM, we defined a seven-element hierarchy vector for each participant and hemisphere (V= [1, 2, 3, …, 7]), whose elements refer to the hierarchical level of the corresponding ROI. The random effect was specified as in equation 1. PF values were standardized before LMEM analysis. This model tests the significance of PF changes along the specified hierarchy. An analogous analysis was applied to CT scores of those seven ROIs.

To statistically assess the effect of eight resting-state networks on PFs, we used a recently released, multi-modal parcellation of the human cortex (Glasser et al., 2016), identified the PF for each cortical parcel of a participant, averaged across parcels within a RSN for that participant according to Ito et al. (Ito et al., 2017), and obtained eight PF values corresponding to eight RSNs for each hemisphere and participant. We specified the PF as a response variable, and a categorical variable comprising eight network categories ('VIS', 'AUD', 'SOM', 'DAN', 'FPN', 'VAN', 'DMN', 'CON') as a fixed effect, for LMEM analysis. The random structure was defined as in equation 1. Next, we applied ANOVA on LMEM fit and computed F-stat for the fixed effect. A similar analysis was performed to test the effect of RSNs on CT scores.

All statistical analyses were conducted in Matlab version 9.5 (R2018b). We used the "fitlme" function to perform the LMEM analysis.

Data availability: All data used for this study are publicly available (https://data.donders.ru.nl/collections/di/dccn/DSC_3011020.09_236?1).

Acknowledgments

The authors would like to thank Peter Hagoort, who initiated and financed the MOUS project, as well as the MOUS-team that collected, and made publicly available, the data used for this study.

Competing Interests

The authors declare that they have no competing interests.

References

Bahramisharif, A., van Gerven, M.A.J., Aarnoutse, E.J., Mercier, M.R., Schwartz, T.H., Foxe, J.J., Ramsey, N.F., Jensen, O., 2013. Propagating neocortical gamma bursts are coordinated by traveling alpha waves. J. Neurosci. 33, 18849–18854. doi:10.1523/JNEUROSCI.2455-13.2013

Bell, A.J., Sejnowski, T.J., 1995. An information-maximization approach to blind separation and blind deconvolution. Neural Comput. 7, 1129–1159. doi:10.1162/neco.1995.7.6.1129

Brodmann, K., 1909. Vergleichende Lokalisationslehre der Grosshirnrinde in ihren Prinzipien dargestellt auf Grund des Zellenbaues. Barth.

Burt, J.B., Demirtaş, M., Eckner, W.J., Navejar, N.M., Ji, J.L., Martin, W.J., Bernacchia, A., Anticevic, A., Murray, J.D., 2018. Hierarchy of transcriptomic specialization across human cortex captured by structural neuroimaging topography. Nat. Neurosci. 21, 1251–1259. doi:10.1038/s41593-018-0195-0

Chaudhuri, R., Knoblauch, K., Gariel, M.-A., Kennedy, H., Wang, X.-J., 2015. A Large-Scale Circuit Mechanism for Hierarchical Dynamical Processing in the Primate Cortex. Neuron 88, 419–431. doi:10.1016/j.neuron.2015.09.008

Chiang, A.K.I., Rennie, C.J., Robinson, P.A., van Albada, S.J., Kerr, C.C., 2011. Age trends and sex differences of alpha rhythms including split alpha peaks. Clin. Neurophysiol. 122, 1505–1517. doi:10.1016/j.clinph.2011.01.040

Demirtaş, M., Burt, J.B., Helmer, M., Ji, J.L., Adkinson, B.D., Glasser, M.F., Van Essen, D.C., Sotiropoulos, S.N., Anticevic, A., Murray, J.D., 2019. Hierarchical Heterogeneity across Human Cortex Shapes Large-Scale Neural Dynamics. Neuron 101, 1181–1194.e13. doi:10.1016/j.neuron.2019.01.017

Duarte, R., Seeholzer, A., Zilles, K., Morrison, A., 2017. Synaptic patterning and the timescales of cortical dynamics. Curr. Opin. Neurobiol. 43, 156–165. doi:10.1016/j.conb.2017.02.007

Eickhoff, S.B., Constable, R.T., Yeo, B.T.T., 2018. Topographic organization of the cerebral cortex and brain cartography. Neuroimage 170, 332–347. doi:10.1016/j.neuroimage.2017.02.018

Ermentrout, G.B., Kleinfeld, D., 2001. Traveling electrical waves in cortex: insights from phase dynamics and speculation on a computational role. Neuron 29, 33–44.

Felleman, D.J., Van Essen, D.C., 1991. Distributed hierarchical processing in the primate cerebral cortex. Cereb. Cortex 1, 1–47. doi:10.1093/cercor/1.1.1

Fries, P., 2005. A mechanism for cognitive dynamics: neuronal communication through neuronal coherence. Trends Cogn. Sci. (Regul. Ed.) 9, 474–480. doi:10.1016/j.tics.2005.08.011

Giocomo, L.M., Hasselmo, M.E., 2009. Knock-out of HCN1 subunit flattens dorsal-ventral frequency gradient of medial entorhinal neurons in adult mice. J. Neurosci. 29, 7625–7630. doi:10.1523/JNEUROSCI.0609-09.2009

Giocomo, L.M., Moser, M.-B., Moser, E.I., 2011. Computational models of grid cells. Neuron 71, 589–603. doi:10.1016/j.neuron.2011.07.023

Glasser, M.F., Coalson, T.S., Robinson, E.C., Hacker, C.D., Harwell, J., Yacoub, E., Ugurbil, K., Andersson, J., Beckmann, C.F., Jenkinson, M., Smith, S.M., Van Essen, D.C., 2016. A multi-modal parcellation of human cerebral cortex. Nature 536, 171–178. doi:10.1038/nature18933

Groppe, D.M., Bickel, S., Keller, C.J., Jain, S.K., Hwang, S.T., Harden, C., Mehta, A.D., 2013. Dominant frequencies of resting human brain activity as measured by the electrocorticogram. Neuroimage 79, 223–233. doi:10.1016/j.neuroimage.2013.04.044

Haller, M., Donoghue, T., Peterson, E., Varma, P., Sebastian, P., Gao, R., Noto, T., Knight, R.T., Shestyuk, A., Voytek, B., 2018. Parameterizing neural power spectra. BioRxiv. doi:10.1101/299859

Hill, J., Inder, T., Neil, J., Dierker, D., Harwell, J., Van Essen, D., 2010. Similar patterns of cortical expansion during human development and evolution. Proc. Natl. Acad. Sci. USA 107, 13135–13140. doi:10.1073/pnas.1001229107

Hillebrand, A., Tewarie, P., van Dellen, E., Yu, M., Carbo, E.W.S., Douw, L., Gouw, A.A., van Straaten, E.C.W., Stam, C.J., 2016. Direction of information flow in large-scale resting-state networks is frequency-dependent. Proc. Natl. Acad. Sci. USA 113, 3867–3872. doi:10.1073/pnas.1515657113

Himberger, K.D., Chien, H.-Y., Honey, C.J., 2018. Principles of temporal processing across the cortical hierarchy. Neuroscience 389, 161–174. doi:10.1016/j.neuroscience.2018.04.030

Huntenburg, J.M., Bazin, P.-L., Goulas, A., Tardif, C.L., Villringer, A., Margulies, D.S., 2017. A systematic relationship between functional connectivity and intracortical myelin in the human cerebral cortex. Cereb. Cortex 27, 981–997. doi:10.1093/cercor/bhx030

Huntenburg, J.M., Bazin, P.-L., Margulies, D.S., 2018. Large-Scale Gradients in Human Cortical Organization. Trends Cogn. Sci. (Regul. Ed.) 22, 21–31. doi:10.1016/j.tics.2017.11.002

Ito, T., Kulkarni, K.R., Schultz, D.H., Mill, R.D., Chen, R.H., Solomyak, L.I., Cole, M.W., 2017. Cognitive task information is transferred between brain regions via resting-state network topology. Nat. Commun. 8, 1027. doi:10.1038/s41467-017-01000-w

Jasmin, K., Lima, C.F., Scott, S.K., 2019. Understanding rostral-caudal auditory cortex contributions to auditory perception. Nat. Rev. Neurosci. 20, 425–434. doi:10.1038/s41583-019-0160-2

Keitel, A., Gross, J., 2016. Individual Human Brain Areas Can Be Identified from Their Characteristic Spectral Activation Fingerprints. PLoS Biol. 14, e1002498. doi:10.1371/journal.pbio.1002498

Kiebel, S.J., Daunizeau, J., Friston, K.J., 2008. A hierarchy of time-scales and the brain. PLoS Comput. Biol. 4, e1000209. doi:10.1371/journal.pcbi.1000209

Markov, N.T., Vezoli, J., Chameau, P., Falchier, A., Quilodran, R., Huissoud, C., Lamy, C.,

595 Misery, P., Giroud, P., Ullman, S., Barone, P., Dehay, C., Knoblauch, K., Kennedy, H.,
596 2014. Anatomy of hierarchy: feedforward and feedback pathways in macaque visual
597 cortex. J. Comp. Neurol. 522, 225–259. doi:10.1002/cne.23458
598 Mellem, M.S., Wohltjen, S., Gotts, S.J., Ghuman, A.S., Martin, A., 2017. Intrinsic frequency
599 biases and profiles across human cortex. J. Neurophysiol. 118, 2853–2864.
600 doi:10.1152/jn.00061.2017
601 Michalareas, G., Vezoli, J., van Pelt, S., Schoffelen, J.-M., Kennedy, H., Fries, P., 2016. Alpha-
602 Beta and Gamma Rhythms Subserve Feedback and Feedforward Influences among
603 Human Visual Cortical Areas. Neuron 89, 384–397. doi:10.1016/j.neuron.2015.12.018
604 Muller, L., Chavane, F., Reynolds, J., Sejnowski, T.J., 2018. Cortical travelling waves:
605 mechanisms and computational principles. Nat. Rev. Neurosci. 19, 255–268.
606 doi:10.1038/nrn.2018.20
607 Murray, J.D., Bernacchia, A., Freedman, D.J., Romo, R., Wallis, J.D., Cai, X., Padoa-Schioppa,
608 C., Pasternak, T., Seo, H., Lee, D., Wang, X.-J., 2014. A hierarchy of intrinsic timescales
609 across primate cortex. Nat. Neurosci. 17, 1661–1663. doi:10.1038/nn.3862
610 Oostenveld, R., Fries, P., Maris, E., Schoffelen, J.-M., 2011. FieldTrip: Open source software
611 for advanced analysis of MEG, EEG, and invasive electrophysiological data. Comput Intell
612 Neurosci 2011, 156869. doi:10.1155/2011/156869
613 Penny, W.D., Friston, K.J., Ashburner, J.T., Kiebel, S.J., Nichols, T.E., 2011. Statistical
614 parametric mapping: the analysis of functional brain images. Elsevier.
615 Pernet, C.R., Wilcox, R., Rousselet, G.A., 2012. Robust correlation analyses: false positive and
616 power validation using a new open source matlab toolbox. Front. Psychol. 3, 606.
617 doi:10.3389/fpsyg.2012.00606
618 Schoffelen, J.-M., Hultén, A., Lam, N., Marquand, A.F., Uddén, J., Hagoort, P., 2017.
619 Frequency-specific directed interactions in the human brain network for language. Proc.
620 Natl. Acad. Sci. USA 114, 8083–8088. doi:10.1073/pnas.1703155114
621 Schoffelen, J.-M., Oostenveld, R., Lam, N.H.L., Uddén, J., Hultén, A., Hagoort, P., 2019. A 204-
622 subject multimodal neuroimaging dataset to study language processing. Sci. Data 6, 17.
623 doi:10.1038/s41597-019-0020-y
624 Schoffelen, J.M., Oostenveld, R., Lam, N.H.L., Udden, J., Hultén, A.H., Hagoort, P., 2019.
625 Mother of unification studies, a 204-subject multimodal neuroimaging dataset to study
626 language processing. Donders Repository.
627 Van Essen, D.C., Glasser, M.F., Dierker, D.L., Harwell, J., Coalson, T., 2012. Parcellations and
628 hemispheric asymmetries of human cerebral cortex analyzed on surface-based atlases.
629 Cereb. Cortex 22, 2241–2262. doi:10.1093/cercor/bhr291
630 Van Veen, B.D., van Drongelen, W., Yuchtman, M., Suzuki, A., 1997. Localization of brain
631 electrical activity via linearly constrained minimum variance spatial filtering. IEEE Trans.
632 Biomed. Eng. 44, 867–880. doi:10.1109/10.623056
633 Wagstyl, K., Ronan, L., Goodyer, I.M., Fletcher, P.C., 2015. Cortical thickness gradients in

structural hierarchies. Neuroimage 111, 241–250. doi:10.1016/j.neuroimage.2015.02.036

Wang, X.-J., 2010. Neurophysiological and computational principles of cortical rhythms in cognition. Physiol. Rev. 90, 1195–1268. doi:10.1152/physrev.00035.2008

Zhang, H., Watrous, A.J., Patel, A., Jacobs, J., 2018. Theta and alpha oscillations are traveling waves in the human neocortex. Neuron 98, 1269–1281.e4. doi:10.1016/j.neuron.2018.05.019

Figures

Figure 1. Spatial gradient of peak frequency (PF) across human cortex follows the posterior-anterior hierarchy. (A) Estimating the power spectrum for each cortical region, and identifying peak frequencies after fitting and subtracting the arrhythmic 1/f component. (B) Top panel: correlation between trimmed mean PF (187 participants, 384 ROIs) and ROI's location along the y-axis (posterior to anterior) ($r = -0.84$, $p << 0.001$). Points are colored according to their Z coordinates. Bottom panel: distribution of trimmed mean PFs across 384 cortical ROIs. (C) Top panel: t-values obtained from linear mixed effect modeling of PF as a function of the coordinates of the ROI centroids. Bottom panel: cortical map of the corresponding fixed effect parameters (see equation 2 for details).

Figure 2. The spatial gradient of 1/f components (offset and slope) across human cortex. (A) Top panel: t-values obtained from linear mixed effect modeling of 1/f offset as a function of the coordinates of the ROI centroids. Bottom panel: cortical map of the corresponding fixed effects. (B) LMEM was applied on 1/f slope, analogous to the 1/f offset. The slope and offset of 1/f component were estimated for each ROI and participant, using the FOOOF package (see methods section for further details). (C) Correlation between trimmed mean PFres (187 participants, 384 ROIs) and ROI's location along the y-axis (posterior to anterior) ($r = -0.63$, $p << 0.001$). The residual PF scores (PFres) were obtained after regressing out the contribution of 1/f offset and slope values (fixed effect) from PF, using LMEM. (D) t-values obtained from linear mixed effect modeling of PF as a function of the coordinates of the ROI centroids (LMEM; t-values: $Y = -8.3$, $Z = -4.3$, $Y:Z = -16$; all $p < 0.001$). The cortical maps show the corresponding fixed effects.

Figure 3. Spatial gradient of cortical thickness and its association with corresponding PF values. (A) Top panel: correlation between mean cortical thickness and ROI's location along the y-axis (posterior to anterior) ($r = -0.84$, $p << 0.001$). Bottom panel: cortical map of trimmed mean PF across 384 cortical ROIs. (B) Correlation between trimmed mean PF (187 participants, 384 ROIs) and trimmed mean CT. (posterior to anterior) ($r = -0.84$, $p << 0.001$). (C) Correlation between the trimmed mean PF and the trimmed mean CT, after regressing out the effect of ROI coordinates.

Figure 4. PF and CT variation along the cortex follows anatomical hierarchies. (A) Relationship between the PF/CT gradients and the cortical hierarchies along the anatomically defined visual hierarchy comprising seven regions (V1, V2, V4, MT, DP, TEO, 7A) (PF: $t = -10.1$, $p << 0.001$; CT: $t = 54.9$, $p << 0.001$). (B) Cortical areas were assigned to eight functional resting-state networks comprising three sensory ('VIS', visual; 'AUD', auditory; and 'SOM', somatomotor) and five association ('DAN', dorsal attention; 'FPN', frontoparietal; 'VAN', ventral attention; 'DMN', default mode; and 'CON', cingulo-opercular) networks. (C) PF/CT values per RSN, averaged across corresponding regions (10% trimmed-mean across participants). The significant effect of RSNs for CT and PF variation along the cortex specified by application of ANOVA on corresponding LMEM (PF: F-stats = 264, $p << 0.001$; CT: F-stats = 746, $p << 0.001$). PF values were significantly lower in association RSNs (except for DAN) than in sensory RSNs ($t = -11.1$, $p << 0.001$), whereas CT values were significantly higher in association RSNs than in sensory RSNs ($t = 14.1$, $p<<0.001$). Error bars indicate the SD across areas within an RSN.

Figure 5. Histogram of spectral peaks. Histogram of all detected spectral peaks (across ROIs and participants) delineates the classical frequency bands used in the EEG and MEG literature (theta 3.5–7.5 Hz, alpha 8.5–13 Hz, low-beta 15–25 Hz and high-beta 27.5–34).

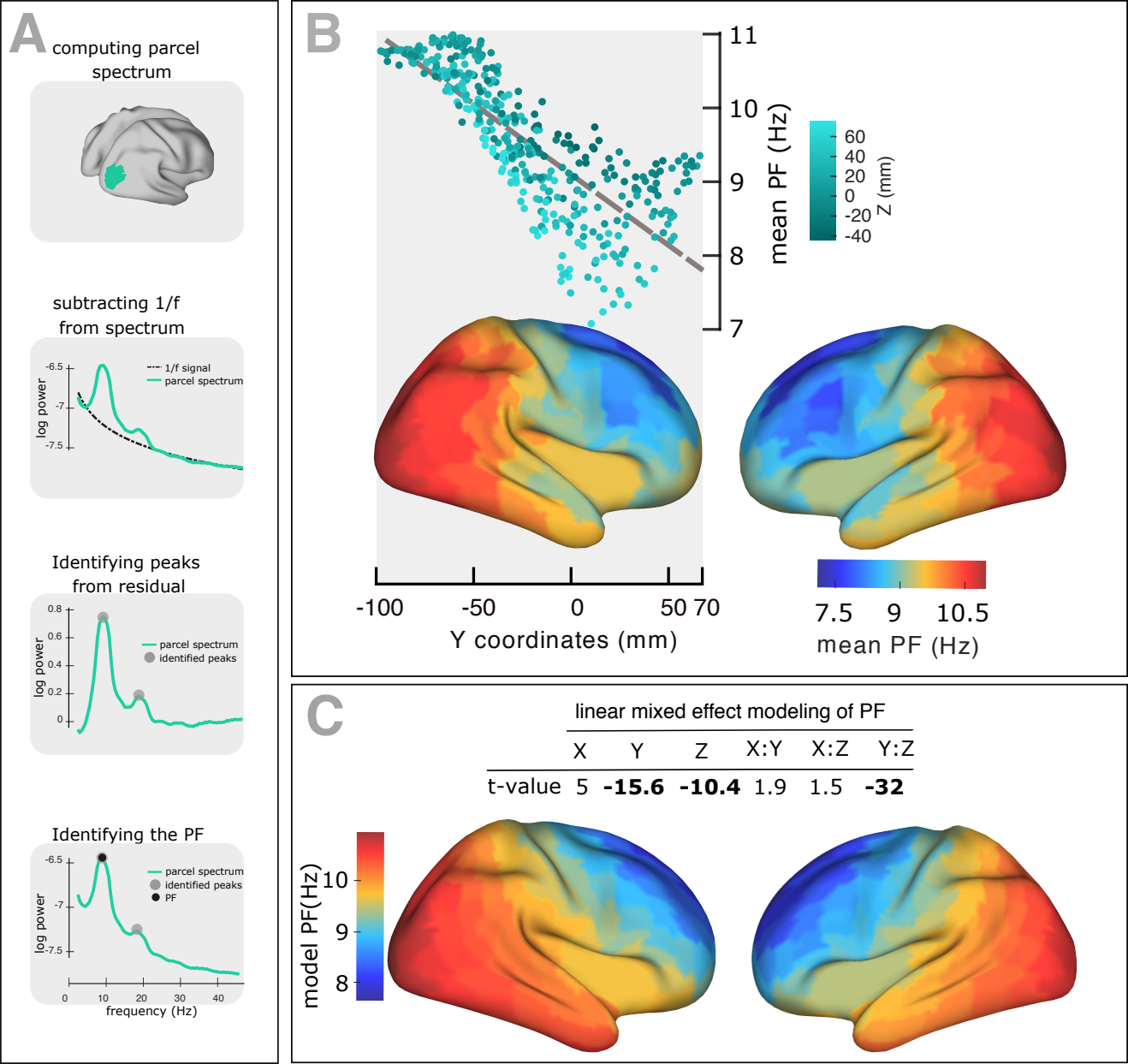
A
computing parcel spectrum
subtracting 1/f from spectrum
1/f signal
parcel spectrum
log power
Identifying peaks from residual
parcel spectrum
identified peaks
Identifying the PF
PF
frequency (Hz)
B
mean PF (Hz)
Z (mm)
Y coordinates (mm)
mean PF (Hz)
C
linear mixed effect modeling of PF
X Y Z X:Y X:Z Y:Z
t-value 5 -15.6 -10.4 1.9 1.5 -32
model PF(Hz)

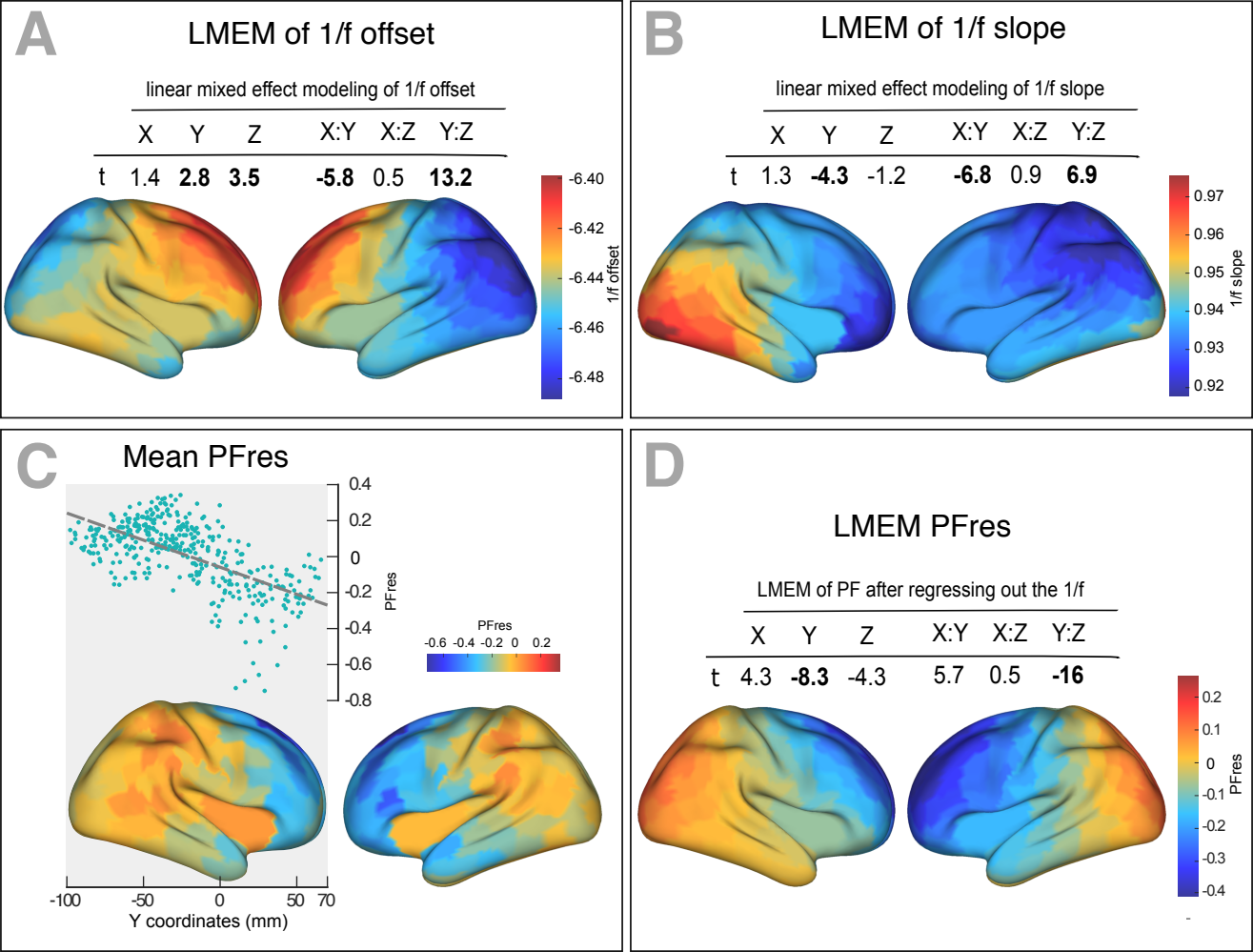
A
LMEM of 1/f offset
linear mixed effect modeling of 1/f offset
X Y Z X:Y X:Z Y:Z
t 1.4 2.8 3.5 -5.8 0.5 13.2
-6.40
-6.42
-6.44
-6.46
-6.48
1/f offset
B
LMEM of 1/f slope
linear mixed effect modeling of 1/f slope
X Y Z X:Y X:Z Y:Z
t 1.3 -4.3 -1.2 -6.8 0.9 6.9
0.97
0.96
0.95
0.94
0.93
0.92
1/f slope
C
Mean PFres
0.4
0.2
0
-0.2
-0.4
-0.6
-0.8
PFres
PFres
-0.6 -0.4 -0.2 0 0.2
-100 -50 0 50 70
Y coordinates (mm)
D
LMEM PFres
LMEM of PF after regressing out the 1/f
X Y Z X:Y X:Z Y:Z
t 4.3 -8.3 -4.3 5.7 0.5 -16
0.2
0.1
0
-0.1
-0.2
-0.3
-0.4
PFres

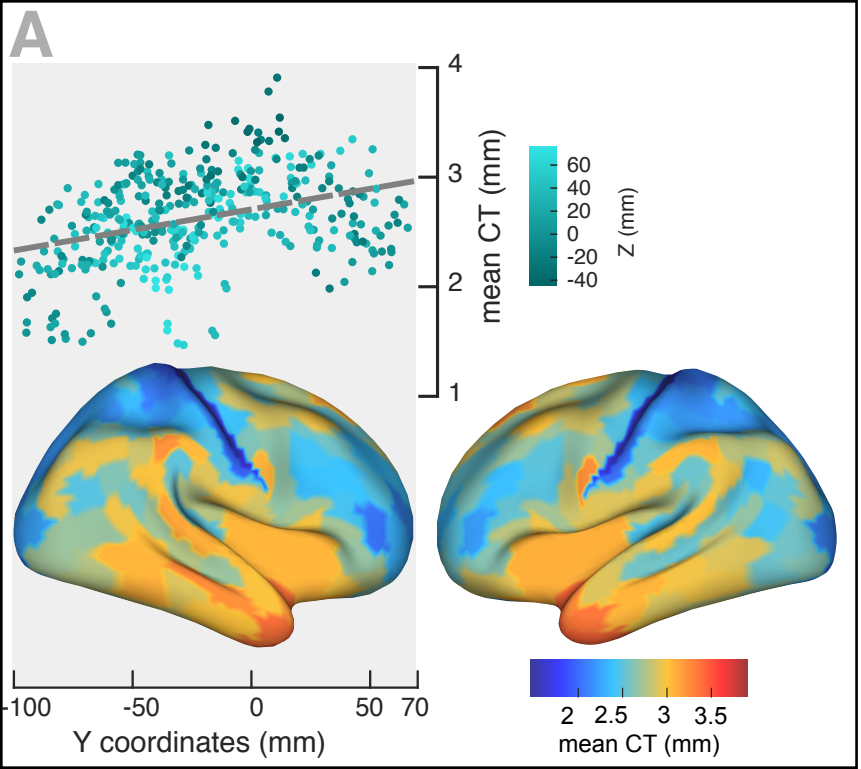
A
4
3
2
1
mean CT (mm)
60
40
20
0
-20
-40
Z (mm)
-100
-50
0
50
70
Y coordinates (mm)
2
2.5
3
3.5
mean CT (mm)

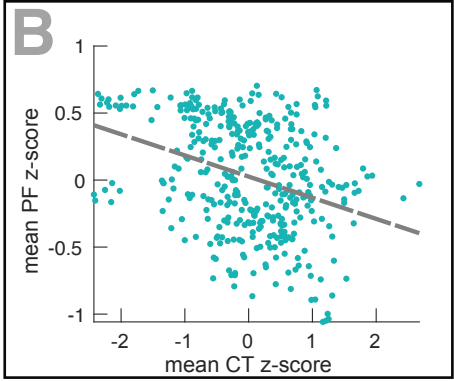
B
1
0.5
0
-0.5
-1
mean PF z-score
-2
-1
0
1
2
mean CT z-score

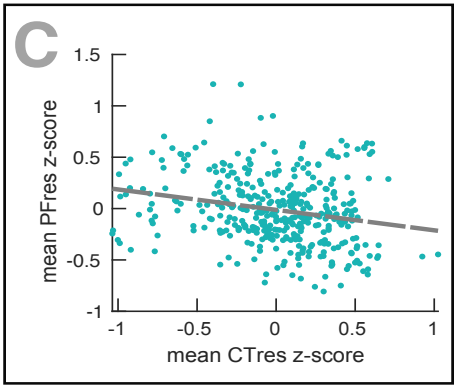
C
1.5
1
0.5
0
-0.5
-1
mean PFres z-score
-1
-0.5
0
0.5
1
mean CTres z-score

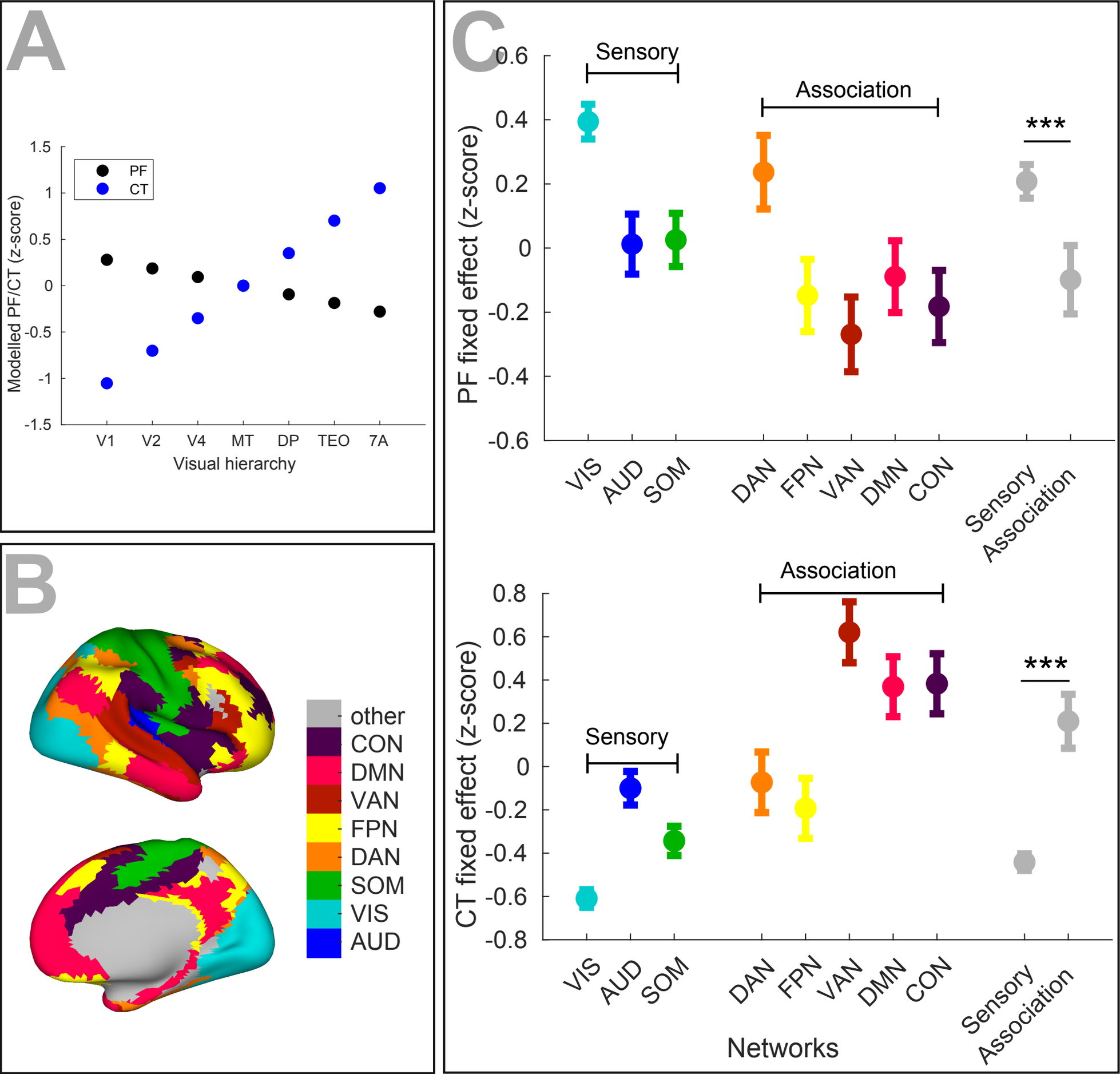
A
PF
CT
Modelled PF/CT (z-score)
1.5
1
0.5
0
-0.5
-1
-1.5
V1
V2
V4
MT
DP
TEO
7A
Visual hierarchy
B
other
CON
DMN
VAN
FPN
DAN
SOM
VIS
AUD
C
Sensory
Association
***
PF fixed effect (z-score)
0.6
0.4
0.2
0
-0.2
-0.4
-0.6
VIS
AUD
SOM
DAN
FPN
VAN
DMN
CON
Sensory
Association
Association
***
Sensory
CT fixed effect (z-score)
0.8
0.6
0.4
0.2
0
-0.2
-0.4
-0.6
-0.8
VIS
AUD
SOM
DAN
FPN
VAN
DMN
CON
Sensory
Association
Networks

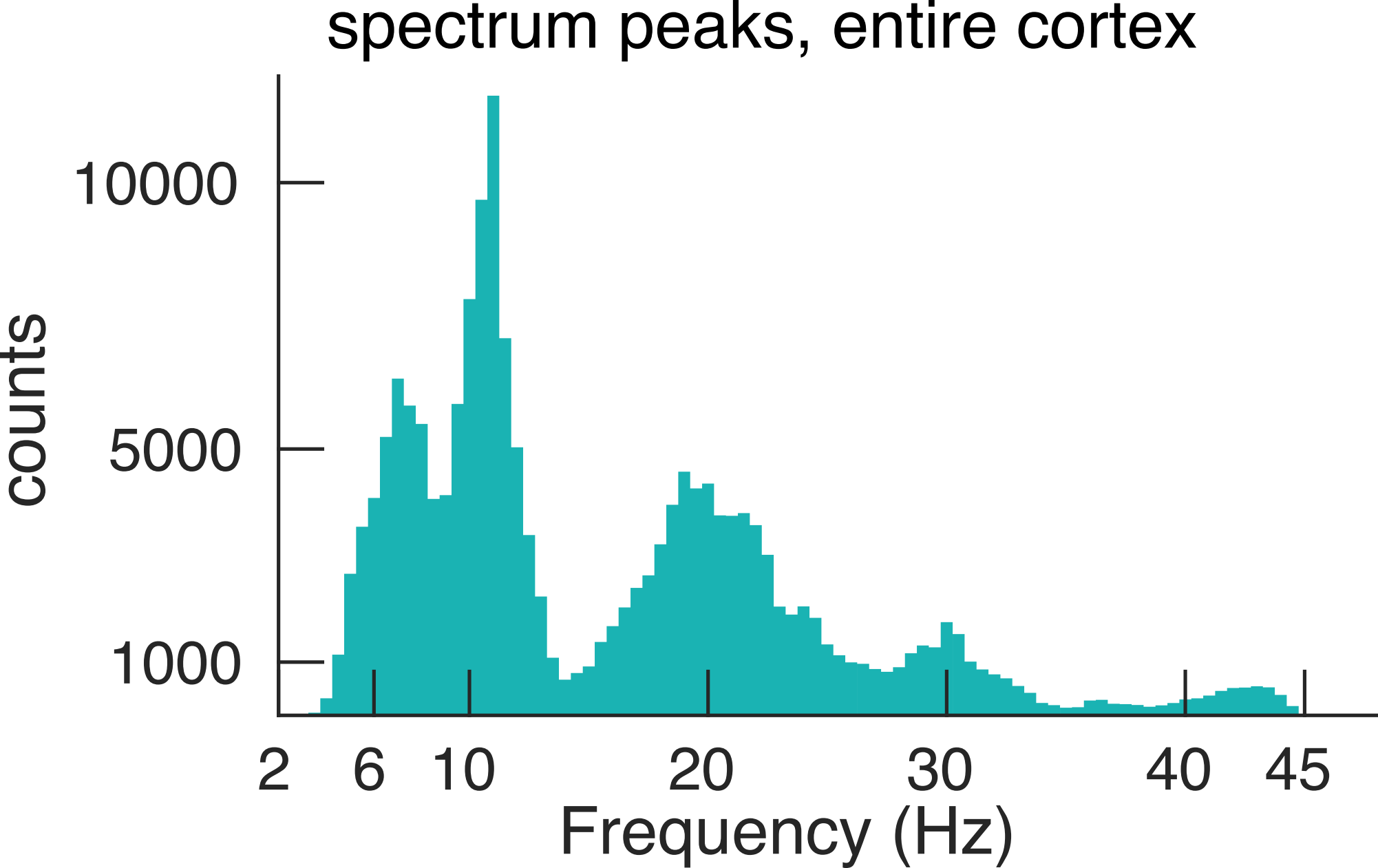
spectrum peaks, entire cortex
10000
5000
1000
counts
2
6
10
20
30
40
45
Frequency (Hz)

SUPPLEMENTAL INFORMATION

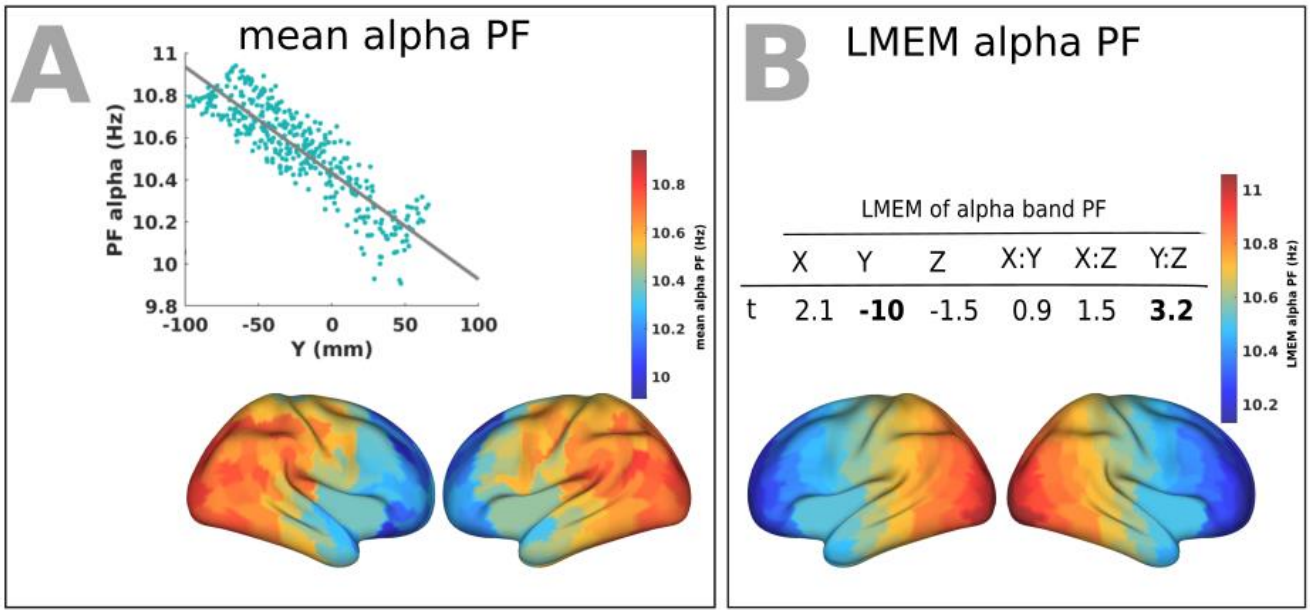

Figure S1. A spatial gradient of alpha-band PFs across human cortex follows the posterior-anterior direction. (A) Top panel: correlation between the trimmed mean of alpha-band PF (187 participants, 384 ROIs) and the ROI's location along the y-axis (posterior to anterior). Bottom panel: distribution of trimmed mean alpha-specific PFs across 384 cortical ROIs. (B) Top panel: t-values obtained from linear mixed effect modeling of alpha-specific PF as a function of the coordinates of the ROI centroids. Bottom panel: cortical map of the corresponding fixed effect parameters (see equation 2 for details).

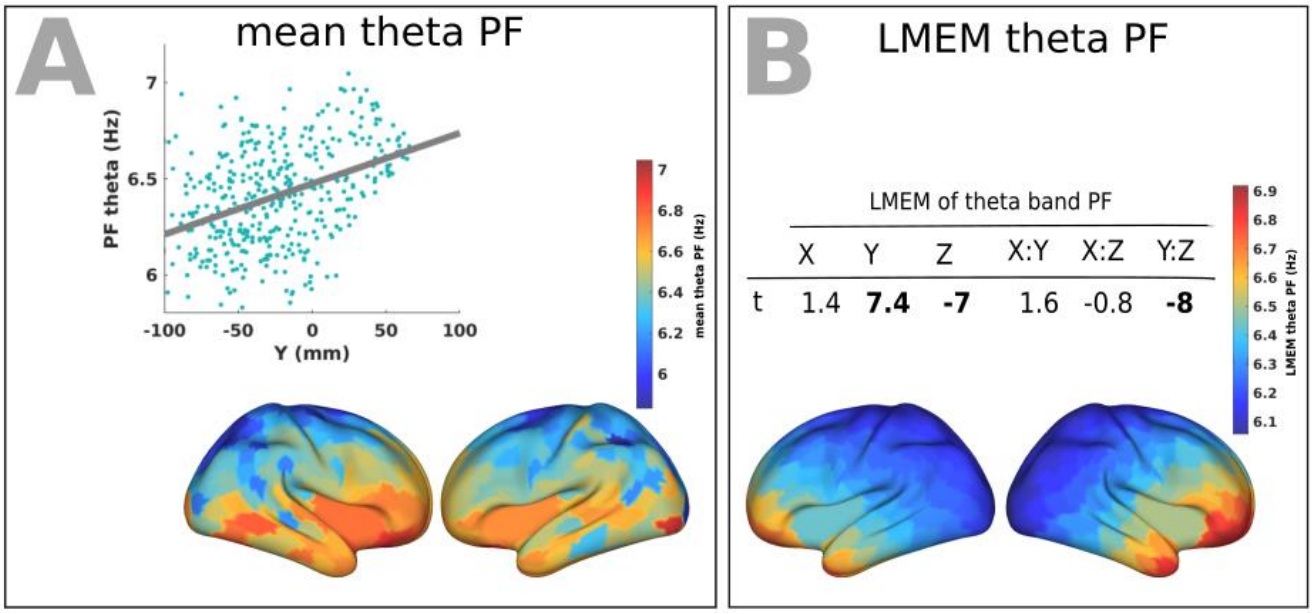

Figure S2. A spatial gradient of theta-band PFs across human cortex largely follows the anterior-posterior direction.

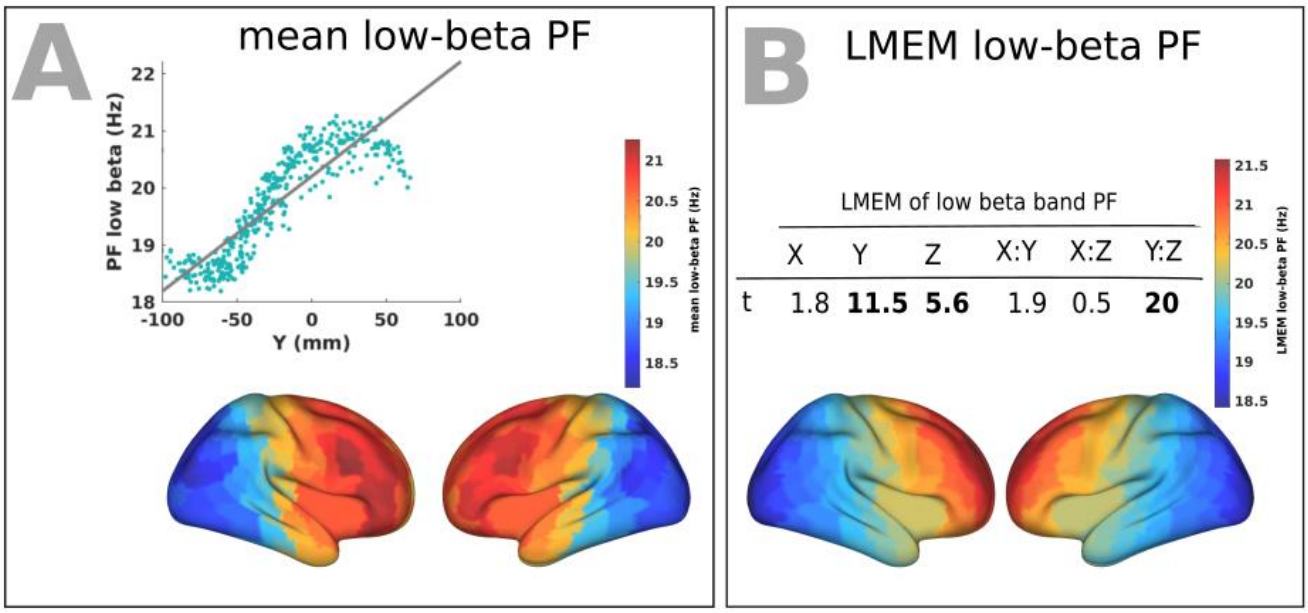

Figure S3. A spatial gradient of low-beta band PFs across human cortex follows the anterior-posterior direction.